Inorganic Chemistry

Article

pubs.acs.org/IC

Morphology-Controlled Synthesis of $W_{18}O_{49}$ Nanostructures and Their Near-Infrared Absorption Properties

Chongshen Guo,*[,†] Shu Yin,[†] Mei Yan,[‡] Makoto Kobayashi,[†] Masato Kakihana,[†] and Tsugio Sato[†]

[†]Institute of Multidisciplinary Research for Advanced Materials, Tohoku University, 2-1-1 Katahira, Aoba-ku, Sendai, 980-8577 Japan

[‡]Department of Chemistry, Graduate School of Science, Tohoku University, Aoba-ku, Sendai, 980-8577 Japan

Supporting Information

ABSTRACT: The morphology-controlled synthesis and near-infrared (NIR) absorption properties of $W_{18}O_{49}$ were systematically investigated for the application of innovative energy-saving windows. Various morphologies of $W_{18}O_{49}$, such as nanorods, nanofibers, nanograins, nanoassembles, nanoplates, and nanoparticles, with various sizes were successfully synthesized by solvothermal reactions using organic alcohols as reaction media and WCl_6, $W(EtO)_6$, and WO_3 solids as the tungsten source. $W_{18}O_{49}$ nanorods of less than 50 nm in length showed the best optical performance as an effective solar filter, which realized high transmittance in the visible region as well as excellent shielding properties of NIR light. Meanwhile, the $W_{18}O_{49}$ nanorods also exhibited strong absorption of NIR light and instantaneous conversion of the absorbed photoenergy to the local heat.

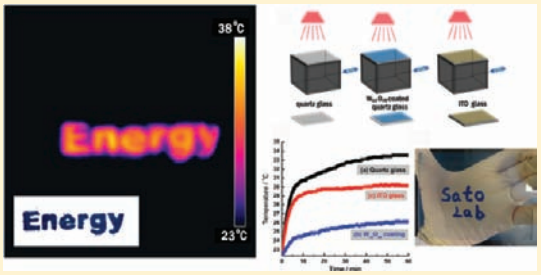

1. INTRODUCTION

Over the past years, tungsten suboxide (WO_{3-x}) nanostructures have been intensively investigated because they possess distinctive physical and chemical properties, which endow them to be effective candidates in various applications, such as field-emission performance,[1,2] photocatalysts,[3] gas sensors,[4] electrochromic devices,[5,6] etc. Among them, $W_{18}O_{49}$ is one of the most investigated ones because of its unusual defect structures and promising properties. Additionally, monoclinic $W_{18}O_{49}$ with the largest oxygen deficiency in $WO_{2.625}$–WO_3 has been reported as the only oxide that can be isolated in a pure form, which is not the case for the other tungsten suboxides (WO_{3-x}).[7] Up to now, several methods have been used to synthesize tungsten suboxides, but the products are all in the one-dimensional form. The growth of quasi-aligned $W_{18}O_{49}$ nanotubes and nanowires has been developed in previous works.[1,8] Wang et al. synthesized $W_{18}O_{49}$ nanowires by annealing WC_x films followed by oxidation.[9] In addition, colloidal $W_{18}O_{49}$ nanorods have been synthesized by pyrolysis $W(CO)_6$ at 250–270 °C in the presence of $Me_3NO{\cdot}2H_2O$ and oleylamine.[10] Consequently, it is highly desired to develop a facile synthetic process of morphology-controlled $W_{18}O_{49}$ (not only in the one-dimensional form) nanoparticles without special equipment, harsh experimental requirements, or poisonous reagent.

In recent years, there has been a strong desire to shield near-infrared (NIR: wavelength of 780–2500 nm) radiation (heat rays) by employing a transparent coating on the windows of automobiles, buildings, etc., in order to reduce the energy consumption for air conditioning and thereby decrease the emission of carbon dioxide. Compared to transitional smart windows having a complex structure and requiring additional power input, such a transparent coating is more energy-saving efficient and simpler, as well as being able to combine two features of energy efficiency (as a result of the curtailing of air conditioning) and indoor comfort (high visible brightness and thermal comfort). For this application, the most active and important element is the absorber, which performs the excellent absorption of NIR rays as well as high visible light transparency.[11−16] In previous works, we found that the tungsten bronze type compounds (M_xWO_3, where M = Cs, Rb, K, Na, etc.) consisting of mixed-valence W ions, such as W^{6+} and W^{5+}, showed excellent NIR shielding properties when dispersed as nanosized particles.[11−17] Because $W_{18}O_{49}$ also consists of mixed-valence W ions, it is expected to show NIR shielding ability.

In a previous work, we synthesized only the $W_{18}O_{49}$ nanorods by a two-step method in which a hydrothermal treatment, followed by an additional reduction process, was needed.[17] The experiment was a little harsh, and the particle size was too big to be an effective candidate as a NIR absorbent. In this paper, we report how the solvothermal approach can be employed to produce $W_{18}O_{49}$ nanomaterials with interesting morphologies, including nanorods, nanofibers, nanospheres, nanoparticles, and even nanoassembles, by systematically changing the kind and concentration of the alcohols and W raw material, and so on, as well as the optical properties of $W_{18}O_{49}$ nanomaterials, such as the NIR absorption, instant conversion of photoenergy to thermal energy, and stimulated solar filter performance. In addition, the morphology and/or size-dependent optical

Received: January 9, 2012
Published: March 23, 2012

   dx.doi.org/10.1021/ic300049j | *Inorg. Chem.* 2012, 51, 4763–4771

performances, together with the possible mechanism for the absorption of NIR light, were also discussed in detail.

2. EXPERIMENTAL SECTION

All of the reagents were of analytical grade and were used as received without further purification. In a typical procedure, a certain amount of a tungsten precursor was dissolved in 50 mL of alcohol to form a 15 mM solution, where WCl_6, $W(C_2H_5O)_6$, and mixtures of the two species with different molar ratios were used as the tungsten precursor and ethanol and propanol were used as the solvents. After that, the solution was transferred into a Teflon-lined autoclave, heated at 200 °C for 24 h, and cooled to room temperature naturally. The product was collected by centrifugation and washed repeatedly with water and ethanol, followed by vacuum drying at 60 °C overnight.

Characterization. The phase compositions of the samples were determined by X-ray diffraction (XRD) analysis (Shimadzu XD-D1) using graphite-monochromatized Cu Kα radiation. The size and shape of the nanoparticles were observed by a transmission electron microscope (JEOL JEM-2010). High-resolution transmission electron microscopy (HRTEM) and selected area electron diffraction (SAED) images were obtained on a ZEISS LEO 922 with an accelerating voltage of 200 kV. The optical properties were measured using a spectrophotometer (JASCO V-670), giving an output of transmittance in the UV, visible, and IR ranges (200−2700 nm), where the $W_{18}O_{49}$ powder was dispersed in a collodion−ethanol mixed solution at a mass ratio of ethanol:collodion:$W_{18}O_{49}$ = 1.0:0.93:0.15. Then, the coating solution was painted on a quartz glass by an applicator with a concave shape and a depth of 12.5 μm. Energy-dispersive X-ray spectroscopy was employed for approximate elemental analyses. Thermogravimetric and differential thermal analyses (TG-DTA, Rigaku TG8101D) were performed on the samples from room temperature to 900 °C with a heating rate of 10 °C/min in air. Thermographic measurements were recorded by a thermographimeter (FLIR System i7).

3. RESULTS AND DISCUSSION

It has been reported that the reduced-type tungsten oxide hydrogen tungsten bronze, which shows mixed chemical states of W^{5+} and W^{6+}, can be fabricated by reducing WO_3 powder with a mild reducing agent because any reducing couple with $E^\circ \leq 0.3$ V can theoretically act as a reducing agent under solvothermal reaction conditions.[18] Alcohols are ideal candidates as mild reducing agents, and were used as reaction solvents to selectively synthesize $W_{18}O_{49}$ nanocrystals in the present study. First, the normal primary alcohols with carbon numbers from 1 to 5, namely, methanol, ethanol, propanol, *n*-butanol, and *n*-pentanol, were selected as solvents. Meanwhile, WCl_6 was used as a tungsten source, and the solvothermal reaction was performed at 200 °C for 24 h. The phase compositions of the products are listed in Table S1 (Supporting Information). The single phase of $W_{18}O_{49}$ ($WO_{2.72}$) could be obtained using methanol, ethanol, propanol, and butanol as solvents, whereas the mixed phase of WO_3 and $W_{18}O_{49}$ was formed using pentanol, indicating that the reducing ability of primary alcohols in this system decreases with increases in the carbon chain length. Furthermore, instead of the pure phase of $W_{18}O_{49}$, a $W_{18}O_{49}$−WO_3 mixture and WO_3 were detected using secondary alcohols, such as 2-propanol and 2-butanol, respectively, indicating that the reducing ability of alcohols is related to not only the carbon chain length but also the position of the hydroxyl.

Figure 1 displays the typical XRD patterns of as-synthesized blue powders resulting from the solvothermal reactions using ethanol and propanol as reaction solvents at 200 °C for 24 h. It can clearly be seen that all of the peaks of the two samples could be well indexed to the monoclinic $W_{18}O_{49}$ phase, although the

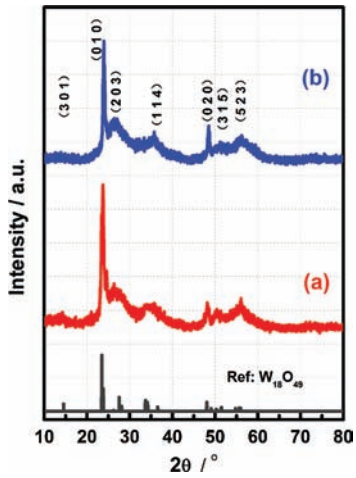

Figure 1. XRD patterns of $W_{18}O_{49}$ nanomaterials synthesized using (a) ethanol and (b) propanol as solvents and 15 mM WCl_6 as a tungsten source under solvothermal reaction at 200 °C for 24 h (reference: $W_{18}O_{49}$, JCPDS No. 712450).

intensity was weak because of the general features of the nanoparticles. Because the tungsten-related oxides have tens of crystal structures, which show similar XRD profiles, XRD results are not enough to prove that the sample is the pure phase of monoclinic $W_{18}O_{49}$. The Raman technique is considered to be a powerful tool for distinguishing the different phases of tungsten oxides, especially for tungsten suboxides.[19−21] Representative Raman spectra of a sample obtained using propanol is shown in Figure 2. There are only two broad

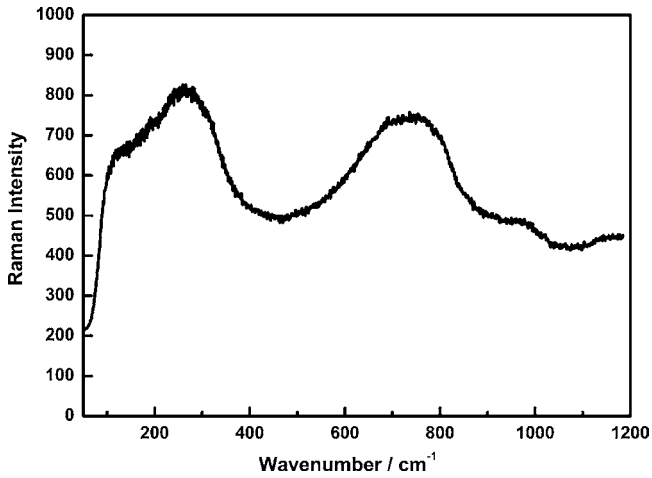

Figure 2. Representative Raman spectra of the $W_{18}O_{49}$ nanocrystal synthesized by solvothermal reaction of a 15 mM WCl_6−propanol solution at 200 °C for 24 h.

bands located at 100−400 and 600−900 nm, which agree well with the general characteristics of $W_{18}O_{49}$ (the $W_{18}O_{49}$ structure contains a wide range of W−O−W bond lengths, so the Raman spectra are expected to lead to very broad and featureless bands).[19] This result also indicates that the synthesized sample was the single phase of monoclinic $W_{18}O_{49}$.

The deep-blue powder synthesized using ethanol exhibited numerous randomly oriented thin nanofibers with diameters of about 10 nm, as shown in Figure 3a. The HRTEM image of a $W_{18}O_{49}$ nanofiber, shown in Figure 3b, indicates clear lattice fringes, suggesting that the nanofiber is a single crystal. In

dx.doi.org/10.1021/ic300049j | Inorg. Chem. 2012, 51, 4763−4771

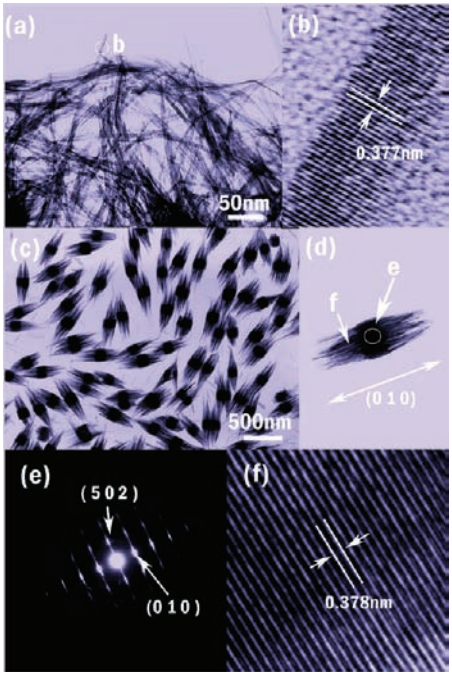

Figure 3. (a) TEM and (b) HRTEM images of the $W_{18}O_{49}$ nanocrystal synthesized by solvothermal reaction of a 15 mM WCl_6–ethanol solution at 200 °C for 24 h, (c and d) TEM images, (e) SAED profile, and (f) HRTEM image of the $W_{18}O_{49}$ nanocrystal synthesized using propanol as the solvent.

addition, the interplanar spacing, determined to be 0.377 nm, agrees with that of the (0 1 0) plane of the monoclinic $W_{18}O_{49}$ crystal, indicating that the growth direction of the nanofiber is along the (0 1 0) plane. This is similar to findings reported in other papers.[22−24] $W_{18}O_{49}$ nanomaterials have been intensively reported in the one-dimensional form, such as nanorods and nanofibers, where growth occurs along the short *b* axis. According to the chemical bonding theory of single crystal growth,[25,26] the fastest growth rate is achieved by linking these WO_6 octahedra to form linear rows along the *b* axis because the $W_{18}O_{49}$ lattice consists of numerous WO_6 octahedra attaching to each other in a complex way by sharing corners and edges. Figure 3c presents a typical TEM image of samples synthesized using propanol. The particles exhibit homogeneous spindlelike particles with widths ranging from 100 to 200 nm and lengths in the range of 300−700 nm. The TEM image of an isolated nanograin reveals that the particle consists of one spherical nanaparticle in the center, from which many nanofibers grow out. SAED recorded from the midpoint of this particle gives evidence that the central part of the particle behaves similarly to a single crystal, and the crystal is stacked by the plane of (0 1 0) along its length direction. The separation of the lattice planes was 0.378 nm, as shown in Figure 3f, which agrees well with the interplanar spacing of (0 1 0). Together with the SAED measurement, it is reasonable to come to the conclusion that the growth direction of a grainlike particle is along (0 1 0).

The chemical composition of the $W_{18}O_{49}$ nanocrystal synthesized using propanol was examined by X-ray photoelectron spectroscopy (XPS). The full range of XPS spectra of the $W_{18}O_{49}$ nanocrystal is shown in Figure 4a. Peaks at binding energies corresponding to oxygen and tungsten are clearly observed, and no impurities other than carbon were observed in the spectra. For tungsten, a complex energy distribution of W 4f photoelectrons was obtained, as shown in Figure 4b. The

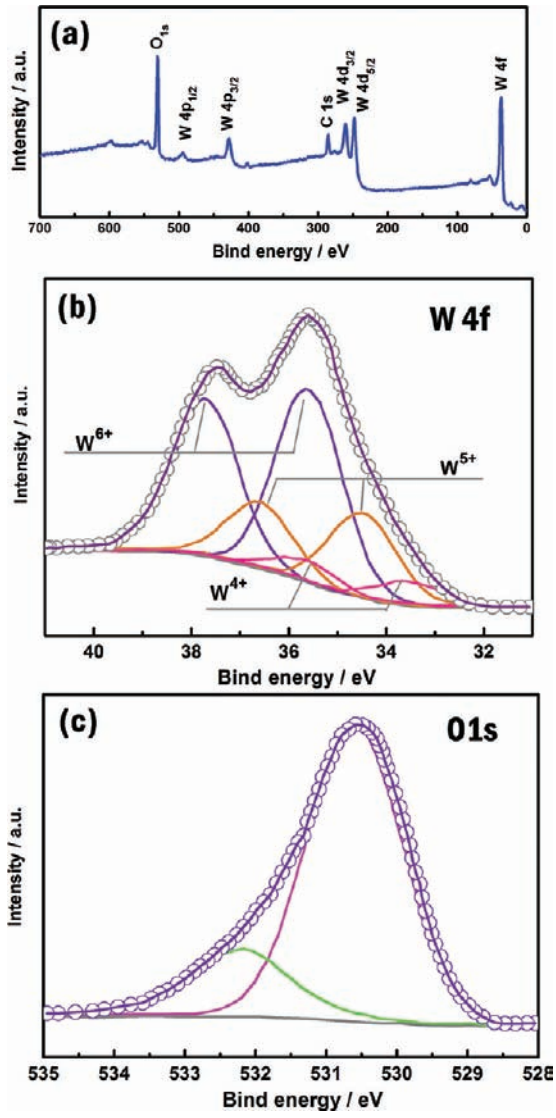

Figure 4. XPS spectra of the $W_{18}O_{49}$ nanocrystal synthesized by solvothermal reaction of a 15 mM WCl_6–propanol solution at 200 °C for 24 h: (a) full-range XPS spectra; (b) deconvolution of the W 4f core-level spectrum with peaks corresponding to W^{6+}, W^{5+}, and W^{4+} oxidation states; (c) O 1s peak showing two chemical bonding states.

W 4f core-level spectrum could be fitted into three doublets, associated with three different oxidation states of W atoms. The main peaks, having W $4f_{5/2}$ at 37.8 eV and W $4f_{7/2}$ at 35.7 eV, are attributable to the W atoms being in a 6+ oxidation state. The second doublet, with a lower binding energy at 34.6 and 36.7 eV, resulted from emission of W $4f_{5/2}$ and W $4f_{7/2}$ core levels from the atoms in an oxidation state of 5+. Furthermore, the third doublet, observed at 33.7 and 335.8 eV, corresponded to the W^{4+} oxidation state. These three oxidation states are the typical oxidation states found in $W_{18}O_{49}$ nanomaterials, as reported previously.[27,28] The photoelectrons from O 1s display a relatively wide and asymmetric peak, with the highest point at 530.5 eV, which could be assigned to the oxygen bond with W atoms in $W_{18}O_{49}$ (Figure 4c). The other peak at a higher photoelectron energy of 532.3 eV may be attributed to the residual water and/or C−O bond originating from the residual adsorbed molecules.

To confirm the formation mechanism of the $W_{18}O_{49}$ nanocrystals under the present solvothermal reaction conditions

dx.doi.org/10.1021/ic300049j | *Inorg. Chem.* 2012, 51, 4763−4771

using ethanol and propanol as a reaction media, the components of the mother liquids after reaction in ethanol and propanol were analyzed by NMR analysis (see Figure S-1 in the Supporting Information). It was found that when pure ethanol was used as a solvent, diethyl ether was formed during the reaction. The 50 mL starting solution consisted of 0.886 mol of ethanol, whereas the solution after reaction consisted of 0.338 mol of ethanol, 0.274 mol of ethyl ether, and 0.274 mol of water. These results suggest that when pure ethanol is used as a reaction solvent, the dehydration condensation reaction of ethanol to form diethyl ether and water occurs, as shown by eq 1. In the case of propanol, a similar etherification reaction, shown in eq 2, was observed; i.e., the starting solution consisted of 0.6535 mol (50 mL) of propanol, whereas the solution after reaction consisted of 0.341 mol of propanol, 0.156 mol of ethyl ether, and 0.156 mol of water.

$$2CH_3CH_2OH \rightarrow CH_3CH_2OCH_2CH_3 + H_2O \quad (1)$$

$$2CH_3CH_2CH_2OH \rightarrow CH_3CH_2CH_2OCH_2CH_2CH_3 + H_2O \quad (2)$$

On the basis of the NMR results, a hydrolytic mechanism for the formation of $W_{18}O_{49}$ nanocrystals was proposed (see Figure 5).

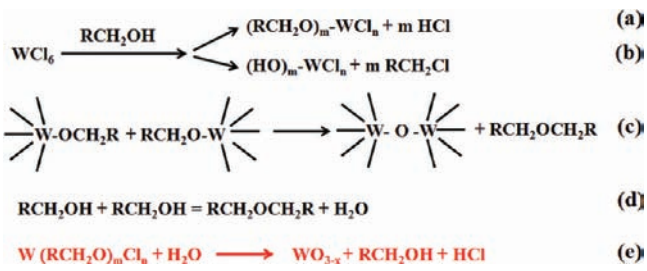

Figure 5. Proposed reaction schemes for the formation of $W_{18}O_{49}$. R represents the alkyl group.

In the initial stage, it was reported that the reaction can yield either HCl and $(RCH_2O)_mWCl_n$ (see Figure 5a) or $(HO)_mWCl_n$ and $mRCH_2Cl$ (see Figure 5b),[29] where R represents the alkyl group. In our case, the strong acidic smell detected during dissolution of tungsten chloride, together with no signal corresponding to RCH_2Cl species in the NMR results, could firmly illustrate that the alcoholysis process is dominating. In the following process, condensation can proceed by two means: (1) two alkoxide fragments condense to form an oxo bridge and an ether molecule (see Figure 5c) or (2) the complex of $(RCH_2O)_mWCl_n$ captures the water molecules released from the etherification reaction to form the tungsten subxoide of $W_{18}O_{49}$. It is well-known that the hydrolysis process more easily produces inorganic oxides compared to the above-mentioned step 1. Therefore, we consider formation of the $W_{18}O_{49}$ nanomaterials in this work mainly via a hydrolysis mechanism.

The thermal behavior of the samples was studied by TG analyses in an air atmosphere with a heating rate of 10 °C/min. The TG plots of two samples synthesized by taking ethanol and propanol as solvents are given in Figure 6. The weight loss up to 250 °C might be assigned to desorption of water, including the loss of surface-adsorbed water (≈90 °C) and structural water elimination (≈250 °C) for both samples. It is noteworthy that the sample synthesized using ethanol exhibited more water loss than that using propanol. This may associate with the result

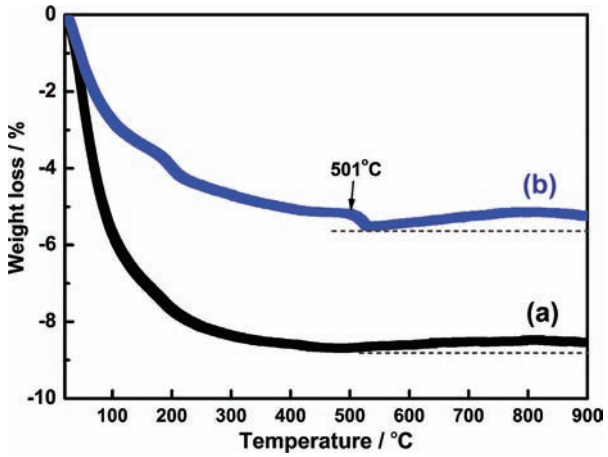

Figure 6. TG patterns of the $W_{18}O_{49}$ nanomaterials synthesized by solvothermal reactions of 15 mM WCl_6 of (a) ethanol and (b) propanol solutions at 200 °C for 24 h.

that there was more water presented in the final ethanol solution (0.274 mol) than in the propanol solution (0.156 mol). At a temperature of about 500 °C, there was an obvious weight loss in the sample obtained using propanol (see Figure 6b). This may be attributed to the loss of absorbed or bonded organics, indicating a strong binding of propanol molecules or related derivates to $W_{18}O_{49}$. In the temperature range of 500–800 °C, a slight weight gain occurred for both samples (Figure 6b) because of oxidation of $W_{18}O_{49}$ to WO_3, as described in eq 3. The XRD analysis confirmed that the resultant powders after TG measurement were WO_3.

$$2W_{18}O_{49} + 5O_2 = 36WO_3 \quad (3)$$

Other than WCl_6, tungsten(VI) ethoxide [$W(EtO)_6$] was also selected as a tungsten source. The solvothermal reactions were performed with varied concentrations of $W(EtO)_6$ ranging from 7.5 to 50 mM at 200 °C for 24 h. The blue powder of $W_{18}O_{49}$ formed in the ethanol solution containing 7.5 mM $W(EtO)_6$ consisted of numerous homogeneous spherical nanoparticles with diameters of around 80 nm (see Figure 7a). Actually, the nanosphere was composed of many small nanoparticles, as shown in Figure 7a, inset. As the concentration of $W(EtO)_6$ increased to 15 mM, interconnected particles with diameters of 200–400 nm were observed (Figure 7b). When the concentration of $W(EtO)_6$ was further increased to 50 mM, the size of the product was also increased, and well-defined and monodispersed microspheres of 0.5–2 μm diameter were formed (Figure 7c). The high-magnification scanning electron microscopy (SEM) image shown in Figure 7d reveals that the surfaces of these microspheres were covered by many thin nanofibers. It is speculated that the great difference in morphologies using different kinds of tungsten precursors, i.e., nanofibers using WCl_6 and nanospheres using $W(EtO)_6$, may be related to the different hydrolysis characteristics of the tungsten source. Unlike WCl_6, which forms a complex of $(RCH_2O)_mWCl_n$ after dissolution, the nucleation and crystal growth process of $W(EtO)_6$ having six equivalent ethoxyls may proceed homogeneouosly to form isotropous spherical particles.

To further investigate the influence of the tungsten precursor on crystal morphology, similar experiments were conducted using mixtures of WCl_6 and $W(EtO)_6$ with varied molar ratios, while keeping the total concentration of tungsten constant. Parts e and f of Figure 7 display the SEM and TEM images of

dx.doi.org/10.1021/ic300049j | Inorg. Chem. 2012, 51, 4763–4771

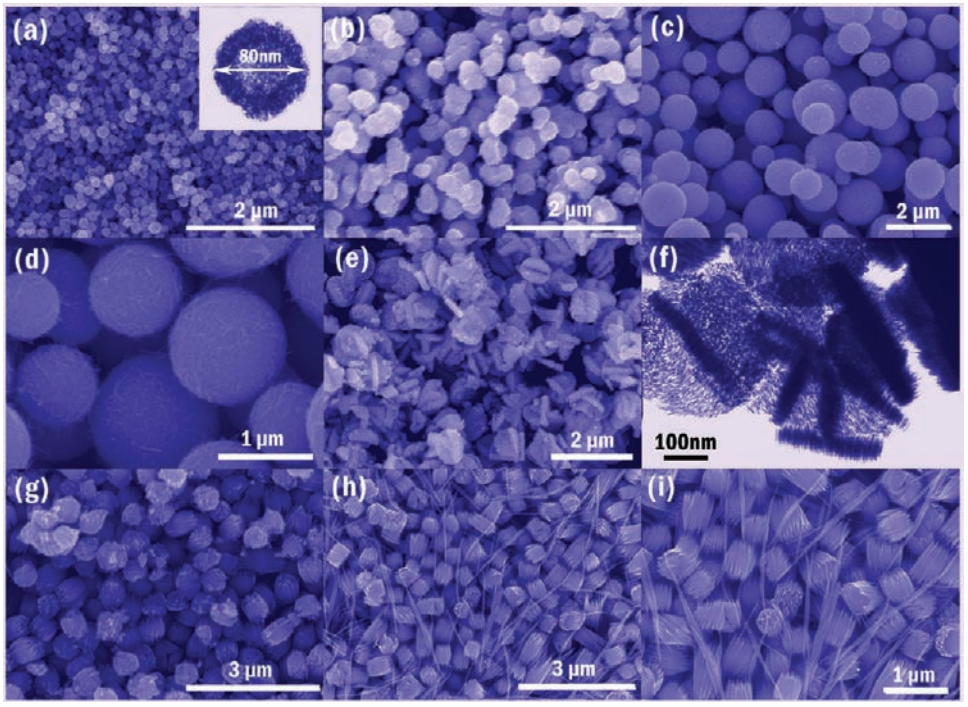

Figure 7. SEM and TEM images of the $W_{18}O_{49}$ nanomaterials synthesized under different reaction conditions. $W_{18}O_{49}$ nanomaterials were also synthesized by solvothermal reactions in an ethanol solution containing (a) 7.5 mM (b) 15 mM, and (c) 50 mM $W(EtO)_6$ at 200 °C for 24 h. The inset in part a shows the corresponding TEM image, and part d is a high-magnification SEM image of part c. SEM and TEM images of samples synthesized by using mixtures of (e and f) 5 mM $W(EtO)_6$ + 10 mM WCl_6, (g) 7.5 mM $W(EtO)_6$ + 7.5 mM WCl_6, and (h and i) 10 mM $W(EtO)_6$ + 5 mM WCl_6 as tungsten sources in propanol (T = 200 °C; t = 24 h).

the $W_{18}O_{49}$ nanoplates obtained using mixtures of 5 mM $W(EtO)_6$ and 10 mM WCl_6 as the tungsten source. The product consisted of cross-platelike particles with sizes ranging from 300 to 600 nm (Figure 7e). The platelike particles were made up of numerous well-aligned nanorods of 30−60 nm thickness (Figure 7f). In contrast, the sample obtained using a mixture of equimolar $W(EtO)_6$ and WCl_6 (7.5 mM) was similar to that shown in Figure 7b, although the particle sizes of 300−500 nm were slightly larger, as shown in Figure 7g. Further increases in the $W(EtO)_6$ content as 10 mM $W(EtO)_6$ and 5 mM WCl_6 resulted in the formation of a high density of nanowires bundled in the form of well-defined rectangular-shaped nanostructures (Figure 7h,i). These results suggest that the morphology of $W_{18}O_{49}$ changes depending on the chemical structure of the tungsten source and the properties of the solvent. The difference in the rate of water generation and reduction ability of the solvent and the difference in the hydrolysis behavior between $W(EtO)_6$ and WCl_6 result in different morphologies of $W_{18}O_{49}$.

In addition to WCl_6 and $W(EtO)_6$, amorphous WO_3 solid was also used as a starting material to conduct similar experiments. The WO_3 solid was prepared as follows: 0.25 g of $Na_2WO_4{\cdot}2H_2O$ was dissolved in 5 mL of deionized water, and then HCl was added to precipitate WO_3. The precipitate was washed six times using deionized water in an ice bath and further rinsed two times using alcohol to remove residual water in the WO_3 solid. Figure 8a shows the TEM image of the sample formed in the ethanol solution. It can be seen that the sample consisted of rodlike nanosized particles of ca. 15−20 nm diameter and 40−80 nm length (Figure 8a). On the other hand, the sample obtained in propanol also exhibited a rodlike shape, but the particle size was smaller than that in ethanol (Figure 8b). Both of these two samples were smaller than those produced using WCl_6 and $W(EtO)_6$.

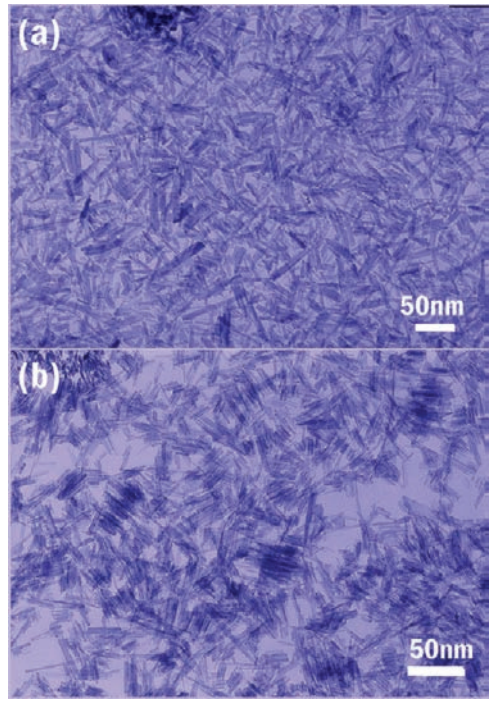

Figure 8. TEM images of samples synthesized in (a) ethanol and (b) propanol using WO_3 solid as a tungsten precursor. (The WO_3 solid was prepared by the hydrolysis of 0.25 g of $Na_2WO_4{\cdot}2H_2O$ in 5 mL of deionized water by adding HCl, followed by washing six times using deionized water in ice bath and rinsing two times using alcohol to remove residual water in WO_3).

dx.doi.org/10.1021/ic300049j | Inorg. Chem. 2012, 51, 4763−4771

For the optical test, the $W_{18}O_{49}$ samples were coated on quartz glass using an applicator after mixing the as-obtained powder with a vis−NIR light transparent binder. Atomic force microscopy (AFM) images of the $W_{18}O_{49}$ films coated on quartz glass were observed to provide detailed information about the surface morphology and homogeneity of the coated films (see Figure 9). It can be seen that the surface layer of the film consisted of uniform nanoparticles.

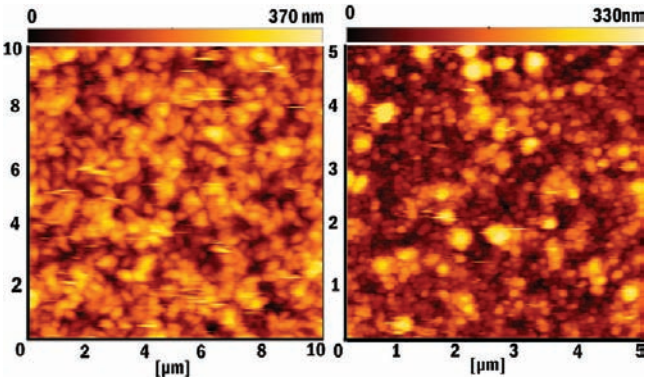

Figure 9. Typical AFM images of films containing the $W_{18}O_{49}$ spherical nanoparticles shown in (a) Figure 3c and (b) Figure 7a.

Figure 10 shows the transmittance and reflectance spectra of films coated with different samples. Tungsten trioxide (WO_3) possesses a wide band gap of 2.62−3.0 eV, being transparent in the visible and NIR light ranges (Figure 10a). In contrast, bulk $W_{18}O_{49}$ shows certain NIR shielding ability, although the NIR shielding performance and visible light transparency were modest, probably because of the large inhomogeneous particles (Figure 10b). When the spindlelike $W_{18}O_{49}$ particles shown in Figure 3c were used, the film showed about 60% transparency of visible light and more than 80% NIR light shielding ability (Figure 10d). In addition, when the $W_{18}O_{49}$ nanofibers synthesized in an ethanol solution with 0.15 mM WCl_6 were used, the best optical properties as a solar filter were obtained; i.e., it achieved high transmittance of about 70% in the visible region as well as nearly 90% of NIR light shielding ability. On the other hand, the value of 100 − T (%) should be the sum of absorption (A %) and reflectance (R %) of light, where T (%) is transmittance. It can be seen that the reflectances of two samples (dashed lines) are quite limited in all wavelength ranges, indicating that the shielding of NIR light by $W_{18}O_{49}$ is mainly caused by absorption of the light.

The size dependence of the optical properties was also investigated, where spherical particles with sizes ranging from 80 nm to 2 μm, together with nanorods obtained using the WO_3 solid, were selected. Figure 11 shows the transmittance spectra of the films prepared using different sizes of $W_{18}O_{49}$ particles. As the size of the nanospheres decreased from 2 μm to 80 nm, the shielding performance of the NIR light increased (Figure 11a−c). Meanwhile, the nanorods consisting of smaller dimensions showed pronounced NIR shielding performance and high transparency of visible light (see Figure 11d,e). In addition, all of the samples listed in Figure 11 also showed very limited reflectance of light in the range of 200−2700 nm (see Figure S-2 in the Supporting Information), indicating that the $W_{18}O_{49}$ nanomaterials realize a strong absorption of NIR light.

It is widely accepted that the optical and electrical properties of functional materials are strongly influenced by their nanostructures, including morphology, size, orientation, and so on. Previous works have found that, in the case of employing reduced-type tungsten oxides for applications as a NIR shielding filer, a sharp size and/or morphology-dependent optical response can be observed,[11−17] owing to the fact that nanosized particles often show unique surface electronic structures and crystallographic defects. For example, characteristic extinction in the NIR region can be realized when the particle size is reduced below a certain region. On the other hand, it is expected that nanorods may exhibit transverse and longitudinal surface plasmon resonances, which correspond to electron oscillations perpendicular and parallel to the rod-length direction, respectively. Therefore, it is a fact that the nanosized one-dimensional $W_{18}O_{49}$ nanocrystal showed excellent and unique characteristics compared to the spherical $W_{18}O_{49}$ and bulk ones (Figure 10). Moreover, the strength and width of the absorption peaks were distinctly enhanced with decreases in the particle size, as shown for another type of NIR shielding material, LaB_6.[30]

Until now, several theories have been proposed to explain the mechanism of NIR shielding by tungsten oxides. Among

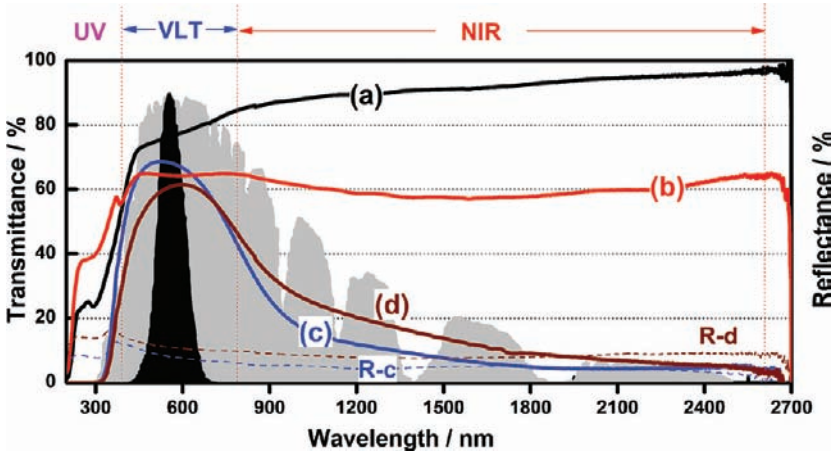

Figure 10. Transmittance spectra of the (a) WO_3, (b) bulk $W_{18}O_{49}$, and (c) $W_{18}O_{49}$ nanofibers shown in Figure 3a and (d) spherical particles shown in Figure 3c. R-c and R-d show the corresponding reflectance spectra of the $W_{18}O_{49}$ nanofibers and $W_{18}O_{49}$ spherical particles, respectively. The black and gray areas indicate the normalized value of the luminous efficiency function and energy wavelength distribution of the solar spectrum at sea level.

dx.doi.org/10.1021/ic300049j | Inorg. Chem. 2012, 51, 4763−4771

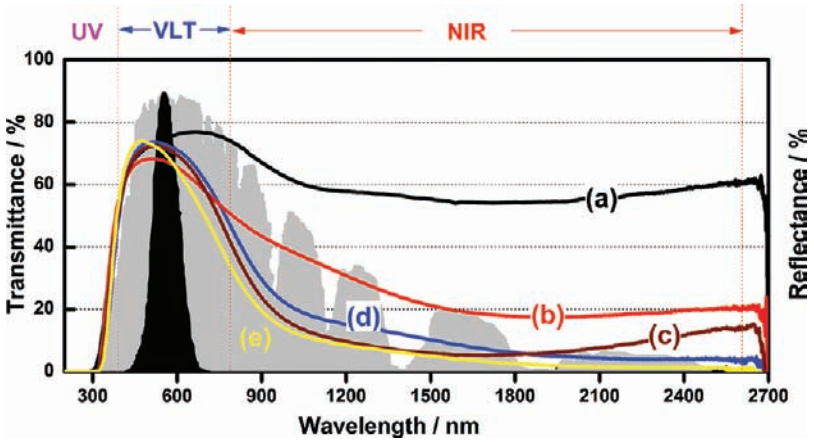

Figure 11. Transmittance spectra of (a) $W_{18}O_{49}$ microspheres with sizes of 0.5−2 μm shown in Figure 7c,d, (b) $W_{18}O_{49}$ nanospheres with sizes of 200−500 nm shown in Figure 7b, (c) $W_{18}O_{49}$ nanospheres with sizes of about 80 nm shown in Figure 7a, (d) $W_{18}O_{49}$ nanorods with lengths of 40−80 nm shown in Figure 8a, and (e) $W_{18}O_{49}$ shorter nanorods shown in Figure 8b. The gray background shows the relative energy wavelength distribution of the solar spectrum at sea level.

them, intervalence charge transfer[31] and small polaron absorption[32] theories are the most widely accepted models. In both cases, NIR shielding is thought to be closely related to the free electrons and oxygen-deficiency-induced small polarons. In the case of disordered films consisting of amorphous or small nanocrystals of tungsten oxides, where the excess electrons are localized and lattice distortions are presented, small polarons are formed when excess electrons polarize their surrounding lattice and localization of the wavelength function takes place essentially to the lattice site. A small overlap occurs between wave functions corresponding to an adjacent site. The absorption of NIR light is related to the polaron transfer by hopping between two neighboring nonequivalent tungsten sites (see Figure 12), denoted as A and B, as follows:[33]

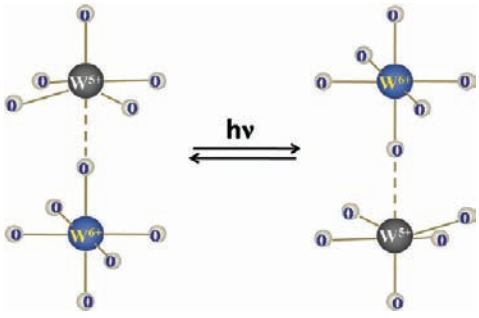

Figure 12. Schematic diagram of polaron hopping between the W^{6+} and W^{5+} states.

$$h\nu + W^{5+}(A) + W^{6+}(B) \rightarrow W^{6+}(A) + W^{5+}(B) + E_{phonon} \quad (4)$$

Of course, the absorption band on the basis of small polaron transitions also includes polaron hopping between the W^{5+} and W^{4+} states.[34]

Experimental evidence for the importance of the oxygen vacancy to the optical properties is extensive. It was observed that WO_{3-x} films exhibit different optical properties for different levels of oxygen deficiency, correlating to a decrease in the ratio of W−O double bonds to single bonds. In a previous work, it was reported that the monoclinic $W_{18}O_{49}$ (i e., $WO_{2.72}$), having the largest amount of oxygen deficiency in the $WO_{2.7}$−WO_3 system, exhibits superior absorption of NIR light compared to other types of tungsten suboxides.[35] On the basis of the above-mentioned mechanism of NIR absorption, it is reasonable to understand that the strong polaron absorption of NIR light resulting from the highly disordered nature in smaller nanocrystals can well explain why the smaller size is preferred in the absorption of NIR light, as shown in Figure 11.

Whether the as-synthesized $W_{18}O_{49}$ nanomaterials have good performance as a solar filter is an essential question, which is closely related to their actual applications in energy-saving windows. Here, a simulated experiment was carried out by irradiating three sealed boxes covered by quartz glass, $W_{18}O_{49}$ nanorods coated with quartz glass, and indium−tin oxide (ITO) glass, to check temperature changes upon irradiation time. The experiment was performed at a room temperature of 22 °C, and a schematic illustration of the simulated experiment is presented in Figure 13A. A 50 W halogen lamp was used as the light source. It can be clearly seen that the inner temperature of the quartz glass set box increased significantly with irradiation time to reach a maximum of about 33.5 °C after 1 h [Figure 13B(a)]. Although the temperature increment could be depressed to a certain degree by substituting quartz glass with commercial ITO glass, prolonged irradiation still caused the temperature to increase remarkably because of its incompleteness of NIR shielding ability for wavelengths of less than 1400 nm. (The optical response of ITO glass is shown in Figure S-3 in the Supporting Information.) In contrast, excellent heat-insulating performance was realized by applying the $W_{18}O_{49}$ nanorods coated with quartz glass; i.e., even after being irradiated for 1 h, the inner temperature increased to only 26.2 °C, which was much lower than the temperatures reached using the quartz glass and ITO glass.

Because the $W_{18}O_{49}$ nanomaterials exhibit strong absorption of NIR light, it is expected to convert the absorbed radiation to local heat directly. To investigate the photothermal conversion properties of the $W_{18}O_{49}$ nanomaterials, the $W_{18}O_{49}$ nanorods shown in Figure 8b were put on a paper and then irradiated by a 50 W halogen lamp for 10 s. The temperature distribution was recorded by thermographic analysis. The inset in Figure 14 shows the image of powder on the paper. The measurement was performed at an ambient temperature of 23 °C. Within

dx.doi.org/10.1021/ic300049j | Inorg. Chem. 2012, 51, 4763−4771

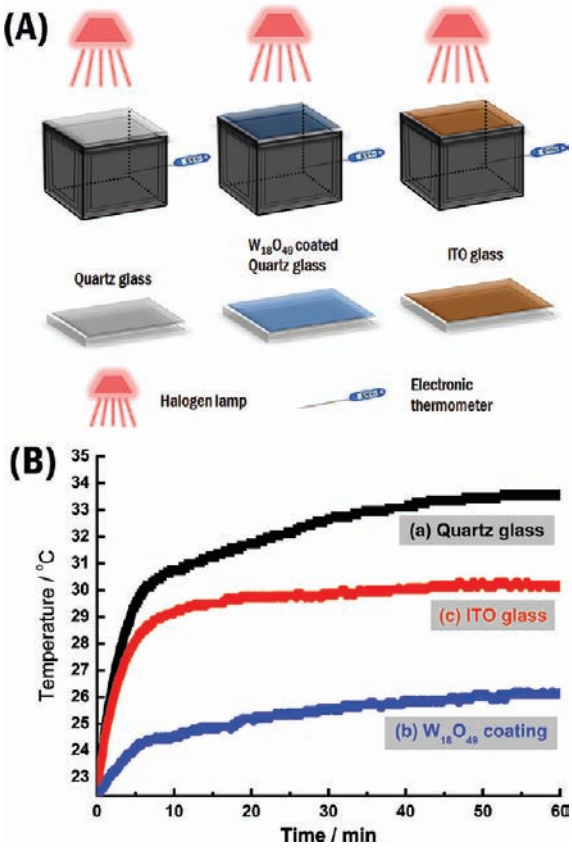

Figure 13. (A) Schematic illustration of the simulated experiment. Sealed boxes with a facet covered by quartz glass, $W_{18}O_{49}$ nanorods coated with quartz glass, and ITO glass were irradiated by a 50 W halogen lamp, and the temperature changes were determined by an electronic thermometer. (B) Time dependence of the temperature in the box.

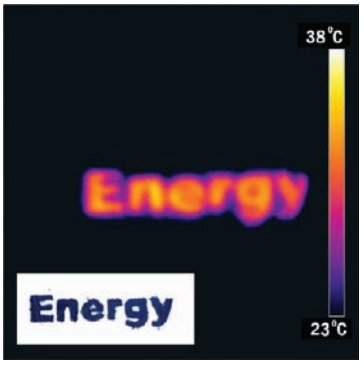

Figure 14. Thermographic images of the $W_{18}O_{49}$ nanorods on the paper. The sample was irradiated by a 50 W halogen lamp for 10 s. The inset shows the shape of $W_{18}O_{49}$ powder on the paper.

only 10 s, the temperature of the powder increased from 23 to 36.5 °C, whereas the temperature of the paper around the sample did not change very much (Figure 14), indicating the quick conversion of absorbed NIR light energy to local heating energy on the $W_{18}O_{49}$ nanorods.

4. CONCLUSION

$W_{18}O_{49}$ nanocrystals with controlled size and morphologies have been successfully fabricated using a facile and novel solvothermal process, in which ethanol and propanol were confirmed to be effective soft reducing solvents and WCl_6, $W(EtO)_6$, and WO_3 solids were selected as starting materials. The NIR absorption properties were improved with decreases in the particle size, and the $W_{18}O_{49}$ nanorods of less than 50 nm in length showed high transmittance of visible light and the strongest absorption of NIR light. It was also confirmed that the $W_{18}O_{49}$ nanorods show superior heat-insulating ability to commercial ITO glass and instantaneous opt-thermal conversion upon NIR irradiation.

■ ASSOCIATED CONTENT

Ⓢ Supporting Information

NMR and optical results. This material is available free of charge via the Internet at http://pubs.acs.org.

■ AUTHOR INFORMATION

Corresponding Author

*E-mail: bigguop@mail.tagen.tohoku.ac.jp. Tel. and fax: +81-22-217-5598.

Notes

The authors declare no competing financial interest.

■ ACKNOWLEDGMENTS

This research was supported, in part, by the Management Expenses Grants for National Universities Corporations from the Ministry of Education, Culture, Sports and Science for Technology of Japan (MEXT), and by the Adaptable and Seamless Technology transfer Program through target-driven R&D, JST, and Grant-in-Aid for Science Research (No. 23241025).

■ REFERENCES

(1) Li, Y.; Bando, Y.; Goldberg, D. *Adv. Mater.* **2003**, *15*, 1294.
(2) Liu, F.; Mo, F. Y.; Jin, S. Y.; Li, L.; Chen, Z. S.; Sun, R.; Chen, J.; Deng, S. Z.; Xu, N. S. *Nanoscale* **2011**, *3*, 1850.
(3) Kojin, F.; Mori, M.; Morishita, T.; Inagaki, M. *Chem. Lett.* **2006**, *35*, 388.
(4) Khyzhun, O. Y.; Solonin, Y. M. *Powder Metall. Met. Ceram.* **2000**, *39*, 287.
(5) Thangala, J.; Chen, Z.; Chin, A.; Ning, C. Z.; Sunkara, M. K. *Cryst. Growth Des.* **2009**, *9*, 3177.
(6) Hong, K.; Xie, M.; Hu, R.; Wu, H. *Appl. Phys. Lett.* **2007**, *90*, 173121.
(7) Remškar, M.; Kovac, J.; Viršek, M.; Mrak, M.; Jesih, A.; Seabaugh, A. *Adv. Funct. Mater.* **2007**, *17*, 1974.
(8) Zhou, J.; Ding, Y.; Deng, S. Z.; Gong, L.; Xu, N. S.; Wang, Z. L. *Adv. Mater.* **2005**, *17*, 2107.
(9) Wang, S. J.; Chen, C. H.; Ko, R. M.; Kuo, Y. C.; Wong, C. H.; Wu, C. H.; Uang, K. M.; Chen, T. M.; Liou, B. W. *Appl. Phys. Lett.* **2005**, *86*, 263103.
(10) Lee, K.; Seo, W. S.; Park, J. T. *J. Am. Chem. Soc.* **2003**, *125*, 3409.
(11) Guo, C. S.; Yin, S.; Zhang, P. L.; Yan, M.; Adachi, K.; Chonan, T.; Sato, T. *J. Mater. Chem.* **2010**, *20*, 8227.
(12) Guo, C. S.; Yin, S.; Adachi, K.; Chonan, T.; Sato, T. *Mater. Sci. Eng.* **2011**, *18*, 032014.
(13) Guo, C. S.; Yin, S.; Yan, M.; Sato, T. *J. Mater. Chem.* **2011**, *21*, 5099.
(14) Guo, C. S.; Yin, S.; Sato, T. *Nanosci. Nanotechnol. Lett.* **2011**, *3*, 413.
(15) Guo, C. S.; Yin, S.; Huang, L. J.; Sato, T. *ACS Appl. Mater. Interfaces* **2011**, *3*, 2794.
(16) Guo, C. S.; Yin, S.; Huang, L. J.; Yang, L.; Sato, T. *Chem. Commun.* **2011**, *47*, 8853.
(17) Guo, C. S.; Yin, S.; Huang, Y. F.; Dong, Q.; Sato, T. *Langmuir* **2011**, *27*, 12172.
(18) Ayyappan, S.; Rao, C. N. R. *Mater. Res. Bull.* **1995**, *30*, 947.

(19) Lu, D. Y. *J. Mater. Res.* **2008**, *23*, 3665.
(20) Lu, D. Y.; Chen, J.; Zhou, J.; Deng, S. Z.; Xu, N. S.; Xu, J. B. *J. Raman Spectrosc.* **2007**, *38*, 176.
(21) Liu, F.; Mo, F. Y.; Jin, S. Y.; Li, L.; Chen, Z. S.; Sun, R.; Chen, J.; Deng, S. Z.; Xu, N. S. *Nanoscale* **2011**, *3*, 1850.
(22) Seo, J.; Jun, W.; Ko, S. J.; Cheon, J. *J. Phys. Chem. B* **2005**, *109*, 5389.
(23) Polleux, J.; Pinna, N.; Antonietti, M.; Niederberger, M. *J. Am. Chem. Soc.* **2005**, *127*, 15595.
(24) Jin, Y. Z.; Zhu, Y. Q.; Whirby, R.; Yao, N.; Ma, R.; Watts, P.; Kroto, H.; Walton, D. *J. Phys. Chem. B* **2004**, *108*, 15572.
(25) Zhao, X.; Bao, Z.; Sun, C.; Xue, D. *J. Cryst. Growth* **2009**, *311*, 711.
(26) Yan, X.; Xu, D.; Xue., D. *Acta Mater.* **2007**, *55*, 5747.
(27) Jeon, S.; Yong, K. J. *Nanotechnology* **2007**, *18*, 1.
(28) Leftheriotis, G.; Passacantando, S.; Yianoulis, P.; Siokou, A. *Thin Solid Film* **2001**, *384*, 298.
(29) Houx, N. L.; Pourroy, G.; Camerel., F.; Comet, M.; Spitzer, D. *J. Phys. Chem. C* **2010**, *114*, 155.
(30) Adachi, K.; Miratsu, M. *J. Mater. Res.* **2010**, *25*, 510.
(31) Faughnan, B. W.; Crandall, R. S.; Heyman, P. M. *RCA Rev.* **1975**, *36*, 177.
(32) Schirmer, O. F.; Wittwer, V.; Baur, G.; Brandt, G. *J. Electrochem. Soc.* **1977**, *124*, 749.
(33) Chatten, R.; Chadwick, A. V.; Rougier, A.; Lindan, P. J. D. *J. Phys. Chem. B* **2005**, *109*, 3146.
(34) Lee, S. H.; Cheong, H. M.; Tracy, C. E.; Mascarenhas, A.; Czanderna, A. W.; Deb, S. K. *Appl. Phys. Lett.* **1999**, *75*, 1541.
(35) Takeda, H.; Adachi, K. *J. Am. Ceram. Soc.* **2007**, *90*, 4059.